PAPER

Flexible free-standing hollow Fe_3O_4/graphene hybrid films for lithium-ion batteries†

Ronghua Wang, Chaohe Xu, Jing Sun,* Lian Gao and Chucheng Lin

Flexible free-standing hollow Fe_3O_4/graphene (H-Fe_3O_4/GS) films were fabricated through vacuum filtration and thermal reduction processes, in which graphene formed a three-dimensional conductive network, with hollow and porous Fe_3O_4 spindles being captured and distributed homogeneously. Using the films as binder-free and free-standing electrodes for lithium-ion batteries, H-Fe_3O_4/GS with 39.6 wt % graphene exhibited a high specific capacity (1555 mA h g^{-1} at 100 mA g^{-1}), enhanced rate capability and excellent cyclic stability (940 and 660 mA h g^{-1} at 200 and 500 mA g^{-1} after 50 cycles, respectively). The superior electrochemical performance of this novel material can be attributed to two factors. One is that the three dimensional (3D) graphene network formed is very helpful for keeping H-Fe_3O_4 in good electrical contact. Another is the short transport length for both lithium ions and electrons due to the porous nature which accommodates volume change and favors electrolyte penetration. It is believed that the strategy for preparing free-standing H-Fe_3O_4/GS films presented in this work will provide new insight into the design and synthesis of other metal oxide/GS electrodes for flexible energy storage devices.

1 Introduction

Nowadays, there is a greatly increased demand for clean and efficient energy storage devices due to the ever-rising concerns about limited energy supplies.[1-3] The rechargeable lithium-ion battery (LIB) is one of the most promising energy storage devices owing to its high energy density, long cyclic life and environmental benignity.[4,5] To meet the increasing demand for LIBs with higher energy densities, intensive efforts have been devoted to explore new electrode materials or design novel nanostructures.[6-8] Among the available anode materials, magnetite (Fe_3O_4) is regarded as a very appealing material for next generation LIBs because of its high theoretical capacity (926 mA h g^{-1}), eco-friendliness and natural abundance.[9-11] However, its severe volume expansions (>200%) occurring upon Li^+ insertion and extraction causes the agglomeration of active materials, electrode pulverization and finally loss of electric contact with the current collector. All these factors will lead to serious capacity loss and greatly hinder the practical application.[12,13] Generally, there are two strategies to solve these problems. One focuses on fabricating delicate nanostructures, such as nanocapsules,[14] hollow beads,[15] wires,[16] arrays,[17] nanocubes[18,19] and microflowers[20] to mitigate the pulverization.

Another approach is to construct hybrids with carbon materials to further enhance the structural stability and electric conductivity.

Graphene sheets have high conductivity, large specific surface area and superior mechanical properties, thus are ideal host materials for anchoring nanocrystals.[21,22] Recently, composites of Fe_3O_4 and graphene were successfully prepared as anode materials for LIBs and greatly improved the lithium storage properties.[23-25] For example, Liu and coworkers[25] reported an *in situ* hydrothermal method to synthesize Fe_3O_4/graphene composites, which exhibited a capacity of 650 mA h g^{-1} at 100 mA g^{-1}. Cheng *et al.*[26] synthesized a flexible interleaved Fe_3O_4/graphene composite and obtained a reversible specific capacity of 1026 mA h g^{-1} at 35 mA g^{-1}. In this previous work, electrodes were usually prepared with anode materials and binders for battery testing. Evidently, a polymer binder may block the diffusion channels for ion transportation resulting in the outstanding electric performance of graphene being significantly sacrificed.[27-30]

Up to now, great efforts have been devoted to prepare free-standing and binder-free electrodes based on graphene. For instance, a flexible graphene film was used as a current collector, upon which metal oxides were decorated by chemical deposition[29,31] or a hydrothermal reaction.[32] Such approaches lead to low loading and aggregation of metal oxides, thus the improvement on the overall hybrid electrode performance is limited. Another method is based on vacuum filtration, by which nanoparticles (<50 nm in diameter) can be incorporated into a graphene scaffold.[30,33] Generally, graphene is aligned and

The State Key Lab of High Performance Ceramics and Superfine Microstructure, Shanghai Institute of Ceramics, Chinese Academy of Sciences, 1295 Dingxi Road, Shanghai 200050, P.R. China. E-mail: jingsun@mail.sic.ac.cn; Fax: +86-21-52413122; Tel: +86-21-52414301

† Electronic supplementary information (ESI) available. See DOI: 10.1039/c2ta00753c

tightly compacted in the hybrid films, which greatly prohibits electrolyte diffusion. To enhance ion diffusion kinetics, Kung and coworkers developed a chemical oxidation method to introduce in-plane vacancies in graphene and greatly improved lithium storage properties.[34,35] However, this procedure is time consuming and may destroy the electronic structure of graphene. Therefore, it is still highly desirable to construct a new pore-enriched hybrid structure with uniform distribution of metal oxide for enhancing Li storage performance.

Herein, well-organized free-standing and flexible Fe_3O_4–GS hybrid films are designed, in which graphene forms a three-dimensional conductive network, with hollow and porous spindle-like Fe_3O_4 (H-Fe_3O_4) being captured and distributed homogeneously. H-Fe_3O_4 was chosen to shorten the Li^+ diffusion length with a wall thickness of 10–20 nm. The porous structure is also beneficial to enhance the electrochemical performance due to the large surface area and hollow space to buffer volume expansion.[14] More importantly, H-Fe_3O_4 spindles (40–80 nm in diameter, 200–400 nm in length) can successfully expand the interlayer spacing of graphene sheets. The hybrid film has a loosely layered three-dimensional structure and many new pores exist between the spindles and the graphene. This pore-enriched nanostructure provides not only abundant open channels for ion transport but also sufficient buffer space for volume expansion of Fe_3O_4. Benefiting from the unique architecture, the free-standing H-Fe_3O_4/GS hybrid electrode exhibits significantly enhanced lithium storage properties in terms of higher specific capacities and better cyclic stability compared to traditional electrodes and pure H-Fe_3O_4 electrodes. The flexible free-standing film is expected to play an important role in fabricating flexible energy storage devices.

2 Experimental

2.1 Materials preparation

(a) Preparation of H-Fe_2O_3. Uniform H-Fe_2O_3 was synthesized by a novel wrap–bake–peel approach.[14] First, spindle-shaped FeOOH was prepared by magnetically stirring aqueous $FeCl_3$ at 80 °C for 6 h. After being pre-coated with polyvinylpyrrolidone (PVP), the as-prepared FeOOH was dispersed in a mixed solution containing 500 ml ethanol and 50 ml deionized water. 30 ml ammonium hydroxide (30 wt%) and 1 ml tetraethoxysilane (TEOS) were then added and the mixture was vigorously stirred for 10 h to realize a silica coating. Subsequently, silica shell/hollow hematite nanostructures were produced by heating at 500 °C for 5 h in air. Finally, H-Fe_2O_3 was obtained after removing the silica shell in 0.1 M NaOH solution for 5 h.

(b) Preparation of H-Fe_3O_4/GS hybrid papers. Graphene oxide (GO) was synthesized from graphite by a modified Hummers method.[36] H-Fe_2O_3 can be readily dispersed in water to form a homogeneous suspension. By mixing the H-Fe_2O_3 dispersion with the GO aqueous dispersion under sonication, a homogeneous dispersion was obtained, which was vacuum-filtered using anodisc membrane filters (47 mm in diameter, 0.2 μm). After drying, free-standing and flexible H-Fe_2O_3/GO hybrid films can be obtained after peeling off from the filter

membrane. Thermal reduction of H-Fe_2O_3/GO hybrid films to H-Fe_3O_4/GS was accomplished in a flow of Ar at 600 °C for 1 h.[37,38] To obtain the optimal electrochemical performance, the various graphene contents of 29.7%, 39.6%, 55.2% and 58.7% were used. The samples were named H-Fe_3O_4/GS-1, H-Fe_3O_4/GS-2, H-Fe_3O_4/GS-3 and H-Fe_3O_4/GS-4, respectively. Detailed characterization was carried out on the optimized sample H-Fe_3O_4/GS-2 hereafter. In comparison, pure H-Fe_3O_4 was obtained by reducing H-Fe_2O_3 in a flow of Ar/H_2 (95 : 5) at 350 °C for 1 h.

2.2 Electrode preparation

H-Fe_3O_4/GS hybrid films were directly used as free-standing electrodes without any binder or additive. The mass loading (areal density) was ~1.7 mg cm^{-2} for H-Fe_3O_4/GS. An H-Fe_3O_4/GS-2 traditional electrode, named trad. electrode, was prepared by conventional slurry-coating technology. Specifically, H-Fe_3O_4/GS-2 hybrid films were first ground into powders, which were mixed with carbon black and poly(vinyldifluoride) (PVDF) at a weight ratio of 80 : 10 : 10 in N-methylpyrrolidone (NMP) to form slurries. The homogeneous slurries were then pasted onto a copper current collector and dried under vacuum at 110 °C for 12 h. Another control electrode, named H-Fe_3O_4, was prepared by the same slurry-coating technology. The mass loading was ~1.2 mg cm^{-2} for the trad. electrode and H-Fe_3O_4 electrode.

2.3 Material characterization

The morphology was characterized by transmission electron microscopy (JEM-2100F, JEOL, Tokyo, Japan). Field-emission scanning electron microscopy (FE-SEM) was performed on a JSM-6700F at an acceleration voltage of 10.0 kV. X-ray diffraction (XRD) was carried out on a D/max 2550 V X-ray diffractionmeter with Cu-Kα irradiation at $\lambda = 1.5406$ Å. Thermal gravimetric analysis (TGA) was conducted in air at a heating rate of 10 °C min^{-1}. Raman spectroscopy was recorded on a DXR Raman Microscope with a 532 nm excitation length, Thermal Scientific Corporation, USA. X-ray photoelectron spectroscopy (XPS) analysis was conducted using a Mg Kα (1253.6 eV) monochromatic X-ray source (Axis Ultra DLD, Kratos). N_2 adsorption/desorption isotherms were determined using a Micromeritics ASAP2010 Analyzer (USA). The conductivity of H-Fe_3O_4/GS hybrid films was measured by a four-point probe method in the van der Pauw configuration with an Accent HL5500 System.

2.4 Electrochemical measurements

Cyclic voltammetry (CV) was carried out in the voltage range 0–3.0 V with a scan rate of 0.5 mV s^{-1}. Electrochemical impedance spectroscopy (EIS) measurements were carried out on the samples with a PARSTAT 2273, using a sine wave of 10 mV over a frequency range of 100 kHz–1 Hz. The electrochemical properties of the H-Fe_3O_4/GS composites as the negative electrode were characterized at room temperature. Li foil was used as the counter electrode. The electrolyte was 1 M $LiPF_6$ in a 50 : 50 w/w mixture of ethylene carbonate (EC) and dimethyl carbonate (DMC). Cell assembly was carried out in a glove box with the

This journal is © The Royal Society of Chemistry 2013

J. Mater. Chem. A, 2013, 1, 1794–1800 | 1795

concentrations of moisture and oxygen below 1 ppm. The batteries were measured using a CT2001 battery tester.

3 Results and discussion

The synthesis process for H-Fe$_3$O$_4$/GS hybrid films is illustrated in Scheme 1. Fig. S1† shows TEM images of the mixed dispersion. H-Fe$_2$O$_3$ was uniformly dispersed on the surface of GO. After vacuum filtration, flexible free-standing H-Fe$_2$O$_3$/GO hybrid papers were obtained (Fig. S2†). Finally, H-Fe$_2$O$_3$–GO was reduced to H-Fe$_3$O$_4$/GS by a simple heat treatment. Fig. 1 displays XRD patterns of H-Fe$_2$O$_3$/GO and H-Fe$_3$O$_4$/GS hybrid films. All the diffraction peaks of H-Fe$_2$O$_3$ can be indexed to rhombohedral hematite (α-Fe$_2$O$_3$-JCPDS no. 33-0664). After heat treatment, H-Fe$_2$O$_3$ was successfully transformed into H-Fe$_3$O$_4$ with XRD patterns that indexed well to magnetite (Fe$_3$O$_4$-JCPDS no. 19-0629).

Fig. 2a and b show the TEM images of as-prepared H-Fe$_2$O$_3$. It consists of hollow spindles with diameters of 40–80 nm and lengths of 200–400 nm. The thickness of the spindle wall is about 10–20 nm, which is favorable for lithium ion diffusion. The SAED pattern reveals that the H-Fe$_2$O$_3$ spindles are highly crystalline. The d-spacing is 2.7 Å, which agrees well with the (104) lattice spacing of hematite. Numerous small and irregular pores can be clearly observed in the SEM images (Fig. 2c and d). The porous structure of H-Fe$_2$O$_3$ was further characterized by Brunauer–Emmett–Teller (BET) specific surface area measurements. As shown in Fig. 3a, H-Fe$_2$O$_3$ spindles have type IV nitrogen adsorption and desorption isotherms,[20,39] indicating the presence of mesopores which contribute to a relatively high BET surface area of 37 m^2 g^{-1}. By contrast, H-Fe$_3$O$_4$/GS film (with 39.6 wt% graphene determined by TGA (Fig. S3†), named H-Fe$_3$O$_4$/GS-2) possesses a higher specific surface area, reaching up to 45.9 m^2 g^{-1} (Fig. 3b).

Fig. 4 and 5 display the top-view and cross-section SEM images of H-Fe$_3$O$_4$/GS-2 film, respectively. From the top view, H-Fe$_3$O$_4$ spindles were wrapped by graphene (Fig. 4a and c), and their hollow morphology can be clearly observed in the corresponding backscattered SEM images (Fig. 4b and d). No aggregates were observed, which is consistent with the TEM
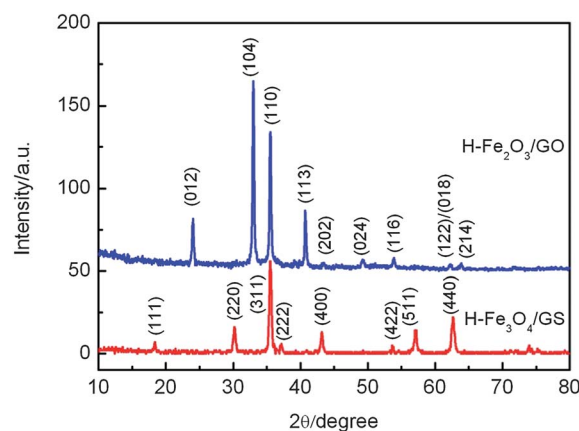
images (Fig. S1†). From the cross-sectional view (Fig. 5a), the thickness of the film is ∼12.3 μm. The inset in Fig. 5a shows that the film had good flexibility. Linked graphene formed a 3D continuous network, which functioned as both a mechanical support and current collector. H-Fe$_3$O$_4$ spindles were embedded into the layered graphene network and distributed homogeneously. Simultaneously, H-Fe$_3$O$_4$ spindles expanded the interlayer spacing between the graphene layers and prevented their agglomeration, which can greatly facilitate electrolyte diffusion compared with the compactly packed structure. Here, many new pores were constructed between the spindles and GS, and this porous nature will facilitate the cross-plane ion diffusivity and provide large surface reaction sites, and is therefore favorable for the electrochemical properties.[40]

To characterize the H-Fe$_3$O$_4$/GS-2 composites in detail, Raman spectroscopy and X-ray photoelectron spectroscopy (XPS) were used to determine the electronic structure and

Fig. 1 XRD curves of the as synthesized H-Fe$_2$O$_3$/GO and H-Fe$_3$O$_4$/GS composites.
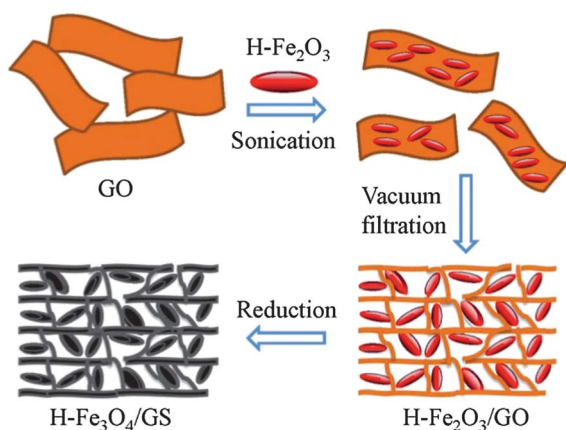
Scheme 1 Schematic illustration of the synthesis of H-Fe$_3$O$_4$/GS hybrid films.
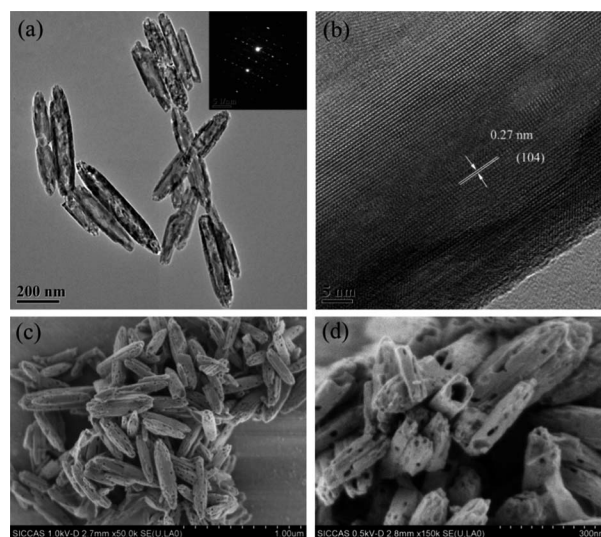

Fig. 2 TEM images (a and b) and FE-SEM images (c and d) of the as-prepared H-Fe$_2$O$_3$; the inset in (a) is the selected area electron diffraction (SAED) pattern of H-Fe$_2$O$_3$.
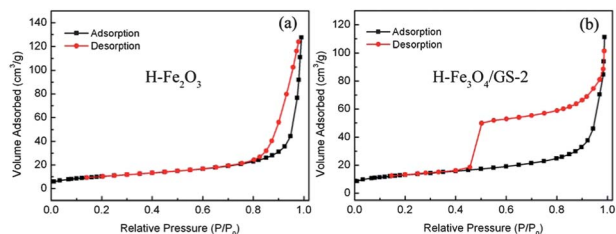
Fig. 3 Nitrogen adsorption and desorption isotherms of (a) H-Fe$_2$O$_3$ and (b) H-Fe$_3$O$_4$/GS-2.
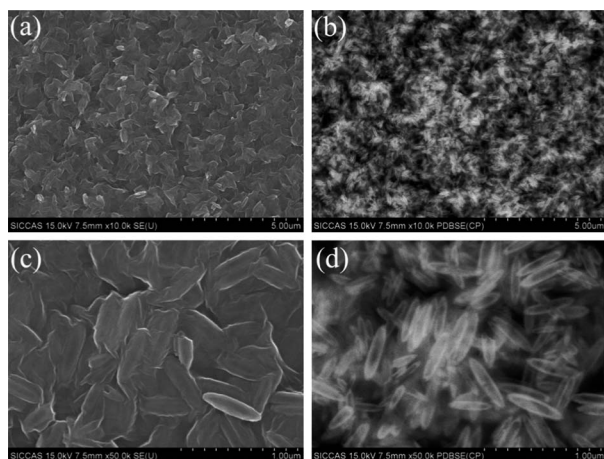

Fig. 4 Top-view SEM images of the H-Fe$_3$O$_4$/GS-2 film (a and c) and the corresponding backscattered SEM images (b and d).
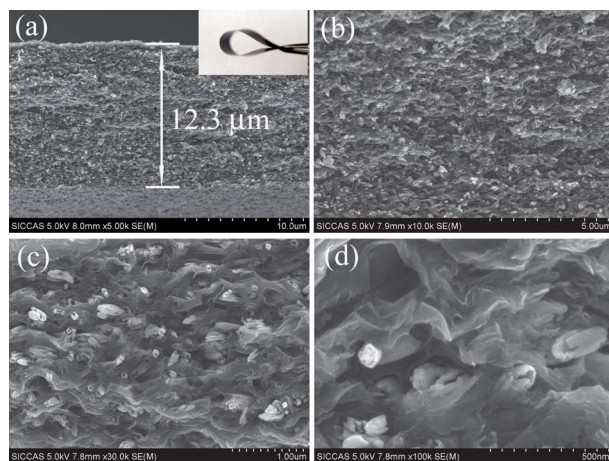

Fig. 5 Cross-section SEM images of the H-Fe$_3$O$_4$/GS-2 film; the inset in (a) is a digital photograph of a H-Fe$_3$O$_4$–GS-2 film showing good flexibility.

composition (Fig. 6). As shown in Fig. 6a, the G bands of H-Fe$_3$O$_4$/GS-2 (1586 cm^{-1}) exhibited red shifts compared with those of pure graphene (1593 cm^{-1}), revealing the n-type doping effect on GS (electron donating effect).[21,41] This indicates significant electronic interactions between GS and H-Fe$_3$O$_4$, which will be of great help for improving the electrochemical performance. XPS was further used to analyze the reduction of
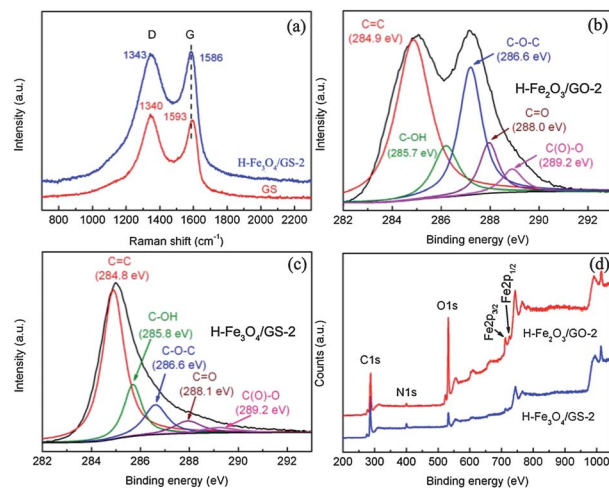

Fig. 6 (a) Raman spectra of GS and H-Fe$_3$O$_4$/GS-2; (b and c) the deconvoluted C 1s spectra of H-Fe$_2$O$_3$/GO-2 and H-Fe$_3$O$_4$/GS-2, respectively; (d) XPS spectra of H-Fe$_2$O$_3$/GO-2 and H-Fe$_3$O$_4$/GS-2.

GO. As shown in Fig. 6b and c, the C 1s spectra were deconvoluted into five different peaks.[42,43] After reduction, the intensities of the peaks for all oxygen-containing functional groups strongly declined compared with those of H-Fe$_2$O$_3$/GO-2 (Fig. 6c). Accordingly, the C/O atomic ratio increased from 1.6 for H-Fe$_2$O$_3$/GO-2 to 8.1 for H-Fe$_3$O$_4$/GS-2 (Fig. 6d, deducting oxygen from Fe$_2$O$_3$ and Fe$_3$O$_4$), demonstrating the large amount of reduction of GO.

Coin cells were made to test the electrochemical performance of H-Fe$_3$O$_4$/GS-2 film. The hybrid film was directly used as a self-supporting electrode (Fig. S4†), without the need of an insulating binder or conducting additive. Cyclic voltammetry (CV) measurements were carried out in the voltage range 0–3.0 V vs. Li$^+$/Li at a scan rate of 0.5 mV s^{-1} (Fig. 7a). In the first cycle, the
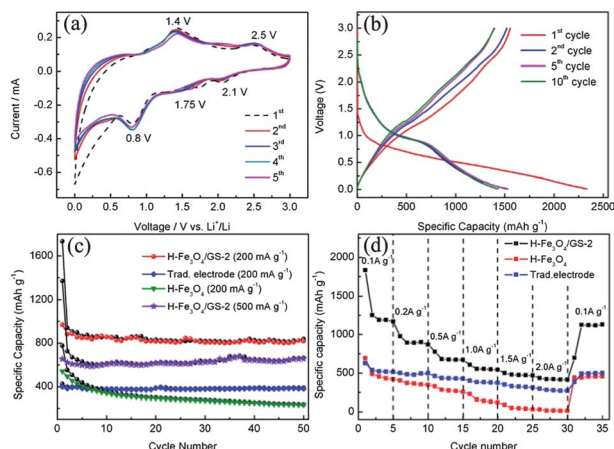

Fig. 7 (a) Cyclic voltammograms for the first five cycles of the as-prepared H-Fe$_3$O$_4$/GS-2 anode film; (b) charge–discharge voltage profiles of H-Fe$_3$O$_4$/GS-2 anode film at a current density of 100 mA g^{-1}; (c) comparative cycle performance of electrodes at a current density of 200 mA g^{-1} and 500 mA g^{-1}; (d) the rate capability of H-Fe$_3$O$_4$/GS-2, the traditional electrode H-Fe$_3$O$_4$/GS-2 and H-Fe$_3$O$_4$ at different current densities.

This journal is © The Royal Society of Chemistry 2013

J. Mater. Chem. A, 2013, **1**, 1794–1800 | **1797**

cathodic peak at ~0.8 V can be attributed to the reduction of both Fe^{3+} and Fe^{2+} to Fe^0 and the irreversible reaction related to the decomposition of electrolyte.[20,44] In this step, the conversion of Fe_3O_4 to Fe and the formation of Li_2O are the main reasons for the irreversible capacity loss during the discharge process. A broad anodic peak at ~1.4 V corresponds to the reversible oxidation of Fe^0 to Fe^{2+} and Fe^0 to Fe^{3+} (reaction 2).[45] In the subsequent cycles, the CV curves were nearly identical, suggesting the good reversibility of the lithium insertion and extraction reactions.[46] Here, graphene can act as a buffer layer for H-Fe_3O_4, and not only alleviates the huge volume changes of H-Fe_3O_4 but also prevents its agglomeration, thereby ensuring the complete reversibility of the lithium intercalation process. In contrast, the peak intensity and integrated area for pure H-Fe_3O_4 dropped rapidly (Fig. S5†), demonstrating that a large capacity loss occurred in the lithium storage process. The reversible reaction occurring with lithium can be summarized as,

$$Fe_3O_4 + 8e^- + 8Li^+ \rightarrow 3Fe^0 + 4Li_2O \qquad (1)$$

$$xLi^+ + Fe^0 + xe^- \rightarrow Li_xFe \qquad (2)$$

Fig. 7b shows representative charge/discharge profiles of H-Fe_3O_4/GS-2 at a current density of 100 mA g^{-1} between 0.01 and 3 V vs. Li$^+$/Li. The gravimetric capacities referred to hereafter are based on the total mass of the composites (including graphene). The first discharge and charge capacities are 2333 and 1555 mA h g^{-1}, respectively. The lithium storage capacities are much higher than the theoretical capacity of Fe_3O_4 owing to the formation of a solid electrolyte interface (SEI) layer and possibly interfacial Li$^+$ storage.[47] From the 2nd to 10th cycles, although slightly decreased, the capacity could still reach up to 1432 mA h g^{-1}.

To highlight the superiority of the unique H-Fe_3O_4/GS-2 free-standing electrode, we also prepared a conventional binder-enriched electrode (with 10 wt% PVDF binder and 10 wt% carbon black) of pure H-Fe_3O_4 and the hybrid H-Fe_3O_4/GS-2 (denoted H-Fe_3O_4 and trad. electrode, respectively) by traditional slurry-coating technology. For pure H-Fe_3O_4, the specific capacity decreased significantly and retained only ~200 mA h g^{-1} at 200 mA g^{-1} after 50 cycles (Fig. 7c). Meanwhile the H-Fe_3O_4/GS-2 traditional electrode displayed much better cyclic performance, stabilizing at ~400 mA h g^{-1} with no apparent capacity loss. This clearly indicates that incorporation of graphene can greatly improve cyclic stability. In contrast, the H-Fe_3O_4/GS-2 free-standing electrode showed the most remarkable performance. Charge/discharge capacities of ~940 mA h g^{-1} at 200 mA g^{-1} were retained with only negligible capacity loss after 50 cycles. The coulombic efficiency rapidly increased to nearly 100% after the first cycle, showing a good reversibility (Fig. S6†). Even at a high current density of 500 mA g^{-1}, the capacity still reached as high as 660 mA h g^{-1}. An additional advantage of the H-Fe_3O_4/GS-2 anode film is the enhancement of the rate capability. The H-Fe_3O_4/GS-2 free-standing electrode delivered very high capacities of 900, 670, 550, 480 and 420 mA h g^{-1} at 200, 500, 1000, 1500 and 2000 mA g^{-1}, respectively (Fig. 7d). These values are much higher than those of the H-Fe_3O_4/GS-2 traditional electrode and the pure

H-Fe_3O_4 electrode. Evidently, the graphene conductive network and free-standing electrode structure contribute significantly to improve the electrochemical properties of H-Fe_3O_4/GS-2 anode film.

In order to gain an in-depth understanding of the advantages of binder-less and free-standing electrodes and the role of graphene, electrochemical impedance spectroscopy (EIS) was employed to investigate the electrochemical reaction kinetics of different electrodes (Fig. 8). The semicircle appearing in the medium frequency range is classically assigned to the charge-transfer resistance (R_{ct}) occurring between active materials and liquid electrolyte.[47–49] The straight line is attributed to the diffusion of lithium ions into electrode materials or so-called Warburg diffusion.[50] For the pure H-Fe_3O_4 electrode (Fig. 8a), R_{ct} is 7.9 Ω before cycling and increased dramatically to 32.2 Ω after ten cycles ($\Delta R_{ct} = 24.3$ Ω), suggesting a considerable degradation of charge transfer kinetics. This may be due to the severe pulverization of H-Fe_3O_4 and loss of electric contact with the current collector.[51–53] In the case of the H-Fe_3O_4/GS-2 traditional electrode (trad. electrode) (Fig. 8b), ΔR_{ct} was 5.6 Ω, much smaller than the pure H-Fe_3O_4 electrode. Evidently, the degradation of charge transfer kinetics was suppressed. This demonstrates graphene effectively accommodated the volume change of H-Fe_3O_4 and prevented its agglomeration during cycling. Compared with the trad. electrode, R_{ct} of the H-Fe_3O_4/GS-2 free-standing electrode was smaller (18.9 Ω) and had a negligible increase after ten cycles ($\Delta R_{ct} = 1.1$ Ω). Apparently, free-standing and binder-free electrodes possess great advantages compared with traditional electrodes. On one hand, the charge transfer kinetics were promoted due to the avoidance of an electrically insulating polymer binder. On the other hand, the specially designed free-standing film, integrating H-Fe_3O_4 and a current collector into one flexible film, ensured durable electric contact of H-Fe_3O_4 with the current collector (graphene). It is noteworthy that the H-Fe_3O_4/GS-2 free-standing electrode displayed a larger phase angle of the Warburg region compared with the other two

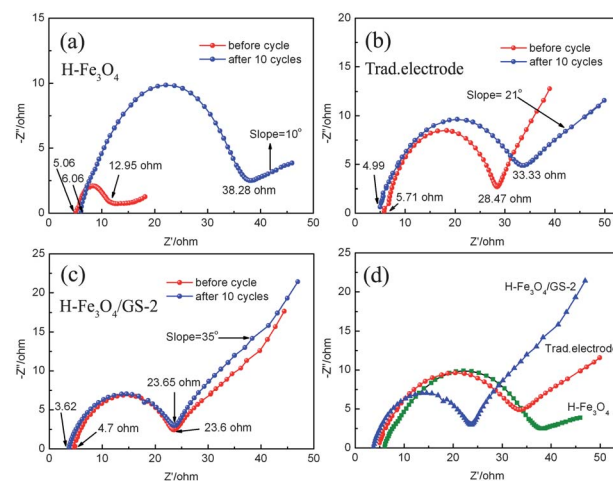**Fig. 8** Nyquist plots of (a) H-Fe_3O_4, (b) H-Fe_3O_4/GS-2 traditional electrode, and (c) H-Fe_3O_4/GS-2 free-standing electrode before and after ten cycles at a constant current density of 100 mA g^{-1}; (d) comparative Nyquist plots of the three electrodes after ten cycles at 100 mA g^{-1}.

electrodes after cycling (Fig. 8d), suggesting higher lithium ion conductivity and enhanced electrode reaction kinetics.[54] This may be a benefit of the porous structure of the hybrid film, which offers abundant open channels for fast ion transport. The above synergetic effect favors a large capacity as well as superior cycle performance of H-Fe$_3$O$_4$/GS-2.

To further understand the effect of the H-Fe$_3$O$_4$/graphene ratio on electrochemical performance, materials with different relative contents of H-Fe$_3$O$_4$ and graphene were prepared. The graphene contents used were 29.7%, 39.6%, 55.2% and 58.7% for H-Fe$_3$O$_4$/GS-1, H-Fe$_3$O$_4$/GS-2, H-Fe$_3$O$_4$/GS-3 and H-Fe$_3$O$_4$/GS-4, respectively (Fig. S3†). The charge/discharge capacities of samples at 200 mA g^{-1} over 50 cycles are plotted in Fig. 9a. For H-Fe$_3$O$_4$/GS-1, serious capacity loss occurred during cycling and only ~550 mA h g^{-1} was retained after 50 cycles. In the case of H-Fe$_3$O$_4$/GS-2, the specific capacity was the highest and the cycling performance was much better than that of H-Fe$_3$O$_4$/GS-1. On one hand, the low content of graphene in H-Fe$_3$O$_4$/GS-1 is insufficient to form a continuous conductive network, leading to a relatively low electrical conductivity (Fig. 9d, 9.7 S m^{-1}). On the other hand, the incomplete graphene network cannot act as a physical barrier to prevent the agglomeration of H-Fe$_3$O$_4$ and buffer its volume change during cycling. This is evident in Fig. S7a and b†, in which H-Fe$_3$O$_4$ spindles in close contact were clearly observed. These two aspects lead to the serious capacity loss of H-Fe$_3$O$_4$/GS-1 in the lithium storage process. Upon further increasing the content of graphene in the hybrid, capacities of about 700 and 620 mA h g^{-1} were retained for H-Fe$_3$O$_4$/GS-3 and H-Fe$_3$O$_4$/GS-4, respectively, much lower than that of H-Fe$_3$O$_4$/GS-2. This may be for two reasons. First is that the capacity of pure H-Fe$_3$O$_4$ is higher than that of pure graphene; the theoretical capacity of the hybrid film decreased with increasing content of graphene. Secondly, unlike H-Fe$_3$O$_4$/GS-2, graphene closely stacked and agglomerated in H-Fe$_3$O$_4$/GS-3 and H-Fe$_3$O$_4$/GS-4 (Fig. S7b–d†). The 2D compacted layered structure hindered the diffusion of electrolyte into the hybrid film and resulted in a lower electrochemically active area.

Accordingly, the specific surface area decreased from 45.9 m^2 g^{-1} for H-Fe$_3$O$_4$/GS-2 to 40.2 m^2 g^{-1} (H-Fe$_3$O$_4$/GS-3) and 39.2 m^2 g^{-1} (H-Fe$_3$O$_4$/GS-4) (Fig. 9d and S8†).

Similarly, H-Fe$_3$O$_4$/GS-2 displayed a rate capability much superior to that of other samples (Fig. 9b). H-Fe$_3$O$_4$/GS-2, H-Fe$_3$O$_4$/GS-3 and H-Fe$_3$O$_4$/GS-4 exhibited similar capacity retentions, which were higher than that of H-Fe$_3$O$_4$/GS-1 (Fig. 9c). These measurements confirm that conductivity, specific surface area and relative capacity contributions of the hybrids synergistically affect the electrochemical performance. In this study, H-Fe$_3$O$_4$/GS-2 achieves a good compromise among these three factors, and consequently, possesses superior lithium storage properties as compared to other three samples.

4 Conclusions

A two-step approach was presented for the synthesis of free-standing and flexible H-Fe$_3$O$_4$/GS hybrid film. H-Fe$_3$O$_4$ was uniformly sandwiched between graphene layers. The highly conductive and flexible graphene network functioned as both a mechanical support and an embedded current collector. As binder-free and flexible anode materials for LIBs, the hybrids with the optimized graphene content (39.6%) achieved high reversible capacities of ~660 mA h g^{-1} after 50 cycles at a current density of 500 mA g^{-1}. Moreover, they benefited from the enhanced structural stability and kinetics (electrical and ion conductivity) for lithium storage; the cycling performance and rate capability were significantly improved compared to traditional electrodes and the pure H-Fe$_3$O$_4$ counterpart. The excellent electrochemical performance is ascribed to the 3D flexible graphene network which not only alleviated the huge volume changes but also prevented the electrochemical agglomeration of H-Fe$_3$O$_4$. The loose stacking of graphene layers and their porous nature also provided a large number of surface reaction sites and favored facile penetration by the electrolyte. In addition, the specially designed free-standing film could always keep the active materials in good electric contact. Accordingly, it is believed that the strategy for preparing free-standing H-Fe$_3$O$_4$/GS films proposed by us may result in a new method for the synthesis of other metal oxide/GS electrodes for flexible energy devices.

Acknowledgements

Notes and references

1 B. Koo, H. Xiong, M. D. Slater, V. B. Prakapenka, M. Balasubramanian, P. Podsiadlo, C. S. Johnson, T. Rajh and E. V. Shevchenko, *Nano Lett.*, 2012, **12**, 2429–2435.

2 C. Xu, J. Sun and L. Gao, *J. Mater. Chem.*, 2012, **22**, 975–979.

3 A. M. Chockla, J. T. Harris, V. A. Akhavan, T. D. Bogart, V. C. Holmberg, C. Steinhagen, C. B. Mullins, K. J. Stevenson and B. A. Korgel, *J. Am. Chem. Soc.*, 2011, **133**, 20914–20921.
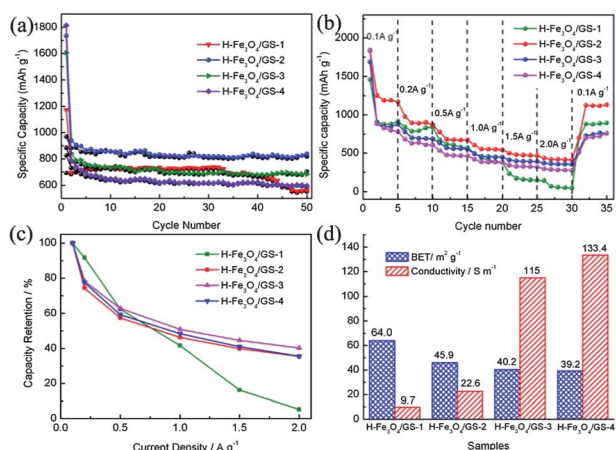
Fig. 9 (a) Cycling performance of H-Fe$_3$O$_4$/GS samples at a current density of 200 mA g^{-1}; (b) rate capability of the samples up to 2 A g^{-1}; (c) capacity retention of the samples at varying current densities; (d) BET and electrical conductivity of H-Fe$_3$O$_4$/GS samples.

4 H. Kim, D.-H. Seo, H. Kim, I. Park, J. Hong, K.-Y. Park and K. Kang, *Chem. Mater.*, 2012, **24**, 720–725.

5 R. S. Ruoff, X. J. Zhu, Y. W. Zhu, S. Murali and M. D. Stollers, *ACS Nano*, 2011, **5**, 3333–3338.

6 R. Li, X. Ren, F. Zhang, C. Du and J. Liu, *Chem. Commun.*, 2012, **48**, 5010–5012.

7 Q. Min, X. Zhang, H. Zhang, F. Zhou and J.-J. Zhu, *Chem. Commun.*, 2011, **47**, 11709–11711.

8 G. Jo, I. Choi, H. Ahn and M. Park, *Chem. Commun.*, 2012, **48**, 3987–3989.

9 E. Kang, Y. S. Jung, A. S. Cavanagh, G. H. Kim, S. M. George, A. C. Dillon, J. K. Kim and J. Lee, *Adv. Funct. Mater.*, 2011, **21**, 2430–2438.

10 W. M. Zhang, X. L. Wu, J. S. Hu, Y. G. Guo and L. J. Wan, *Adv. Funct. Mater.*, 2008, **18**, 3941–3946.

11 Y. Chen, H. Xia, L. Lu and J. M. Xue, *J. Mater. Chem.*, 2012, **22**, 5006–5012.

12 X. Wang, H. Guan, S. Chen, H. Li, T. Zhai, D. Tang, Y. Bando and D. Golberg, *Chem. Commun.*, 2011, **47**, 12280–12282.

13 H. Guan, X. Wang, S. Chen, Y. Bando and D. Golberg, *Chem. Commun.*, 2011, **47**, 12098–12100.

14 H. S. Kim, Y. Piao, S. H. Kang, T. Hyeon and Y. E. Sung, *Electrochem. Commun.*, 2010, **12**, 382–385.

15 Y. Chen, B. H. Song, X. S. Tang, L. Lu and J. M. Xue, *J. Mater. Chem.*, 2012, **22**, 17656–17662.

16 T. Muraliganth, A. V. Murugan and A. Manthiram, *Chem. Commun.*, 2009, 7360–7362.

17 K. Xie, Z. Lu, H. Huang, W. Lu, Y. Lai, J. Li, L. Zhou and Y. Liu, *J. Mater. Chem.*, 2012, **22**, 5560–5567.

18 H. Guan, X. Wang, H. Li, C. Zhi, T. Zhai, Y. Bando and D. Golberg, *Chem. Commun.*, 2012, **48**, 4878–4880.

19 H. Cao, R. Liang, D. Qian, J. Shao and M. Qu, *J. Phys. Chem. C*, 2011, **115**, 24688–24695.

20 S. L. Jin, H. G. Deng, D. H. Long, X. J. Liu, L. A. Zhan, X. Y. Liang, W. M. Qiao and L. C. Ling, *J. Power Sources*, 2011, **196**, 3887–3893.

21 W. Chen, S. Li, C. Chen and L. Yan, *Adv. Mater.*, 2011, **23**, 5679–5683.

22 H. L. Wang, Y. Yang, Y. Y. Liang, L. F. Cui, H. S. Casalongue, Y. G. Li, G. S. Hong, Y. Cui and H. J. Dai, *Angew. Chem., Int. Ed.*, 2011, **50**, 7364–7368.

23 X. D. Huang, X. F. Zhou, K. Qian, D. Y. Zhao, Z. P. Liu and C. Z. Yu, *J. Alloys Compd.*, 2012, **514**, 76–80.

24 C.-T. Hsieh, J.-Y. Lin and C.-Y. Mo, *Electrochim. Acta*, 2011, **58**, 119–124.

25 J.-Z. Wang, C. Zhong, D. Wexler, N. H. Idris, Z.-X. Wang, L.-Q. Chen and H.-K. Liu, *Chem.–Eur. J.*, 2011, **17**, 661–667.

26 G. Zhou, D.-W. Wang, F. Li, L. Zhang, N. Li, Z.-S. Wu, L. Wen, G. Q. Lu and H.-M. Cheng, *Chem. Mater.*, 2010, **22**, 5306–5313.

27 X. Chen, W. Wei, W. Lv, F. Su, Y. He, B. Li, F. Kang and Q.-H. Yang, *Chem. Commun.*, 2012, **48**, 5904–5906.

28 L. Noerochim, J. Z. Wang, S. L. Chou, D. Wexler and H. K. Liu, *Carbon*, 2012, **50**, 1289–1297.

29 H. Gwon, H. S. Kim, K. U. Lee, D. H. Seo, Y. C. Park, Y. S. Lee, B. T. Ahn and K. Kang, *Energy Environ. Sci.*, 2011, **4**, 1277–1283.

30 Z. P. Li, Y. J. Mi, X. H. Liu, S. Liu, S. R. Yang and J. Q. Wang, *J. Mater. Chem.*, 2011, **21**, 14706–14711.

31 F. Xiao, Y. Li, X. Zan, K. Liao, R. Xu and H. Duan, *Adv. Funct. Mater.*, 2012, **22**, 2487–2494.

32 C. Yuan, L. Yang, L. Hou, J. Li, Y. Sun, X. Zhang, L. Shen, X. Lu, S. Xiong and X. W. Lou, *Adv. Funct. Mater.*, 2012, **22**, 2560–2566.

33 S. M. Paek, E. Yoo and I. Honma, *Nano Lett.*, 2009, **9**, 72–75.

34 X. Zhao, C. M. Hayner, M. C. Kung and H. H. Kung, *ACS Nano*, 2011, **5**, 8739–8749.

35 X. Zhao, C. M. Hayner, M. C. Kung and H. H. Kung, *Adv. Energy Mater.*, 2011, **1**, 1079–1084.

36 W. S. Hummers and R. E. Offeman, *J. Am. Chem. Soc.*, 1958, **80**, 1339.

37 K. Y. Xie, Z. G. Lu, H. T. Huang, W. Lu, Y. Q. Lai, J. Li, L. M. Zhou and Y. X. Liu, *J. Mater. Chem.*, 2012, **22**, 5560–5567.

38 Y. J. Chen, G. Xiao, T. S. Wang, Q. Y. Ouyang, L. H. Qi, Y. Ma, P. Gao, C. L. Zhu, M. S. Cao and H. B. Jin, *J. Phys. Chem. C*, 2011, **115**, 13603–13608.

39 X. W. Lou, C. L. Yuan and L. A. Archer, *Adv. Mater.*, 2007, **19**, 3328–3332.

40 Z. Wang, D. Luan, S. Madhavi, Y. Hu and X. W. Lou, *Energy Environ. Sci.*, 2012, **5**, 5252–5256.

41 J. Zhu, T. Zhu, X. Zhou, Y. Zhang, X. W. Lou, X. Chen, H. Zhang, H. H. Hng and Q. Yan, *Nanoscale*, 2011, **3**, 1084–1089.

42 S. Pei and H.-M. Cheng, *Carbon*, 2012, **50**, 3210–3228.

43 Y. H. Ding, P. Zhang, Q. Zhuo, H. M. Ren, Z. M. Yang and Y. Jiang, *Nanotechnology*, 2011, **22**, 215601.

44 Y. Chen, H. Xia, L. Lu and J. Xue, *J. Mater. Chem.*, 2012, **22**, 5006–5012.

45 Y. Z. Piao, H. S. Kim, Y. E. Sung and T. Hyeon, *Chem. Commun.*, 2010, **46**, 118–120.

46 Q. Q. Xiong, J. P. Tu, Y. Lu, J. Chen, Y. X. Yu, Y. Q. Qiao, X. L. Wang and C. D. Gu, *J. Phys. Chem. C*, 2012, **116**, 6495–6502.

47 S.-L. Chou, J.-Z. Wang, D. Wexler, K. Konstantinov, C. Zhong, H.-K. Liu and S.-X. Dou, *J. Mater. Chem.*, 2010, **20**, 2092–2098.

48 Q.-P. Luo, X.-Y. Yu, B.-X. Lei, H.-Y. Chen, D.-B. Kuang and C.-Y. Su, *J. Phys. Chem. C*, 2012, **116**, 8111–8117.

49 Y. J. Mai, X. H. Xia, R. Chen, C. D. Gu, X. L. Wang and J. P. Tu, *Electrochim. Acta*, 2012, **67**, 73–78.

50 X. Jia, Z. Chen, A. Suwarnasarn, L. Rice, X. Wang, H. Sohn, Q. Zhang, B. Wu, F. Wei and Y. Lu, *Energy Environ. Sci.*, 2012, **5**, 6845–6849.

51 X. Wang, X. Cao, L. Bourgeois, H. Guan, S. Chen, Y. Zhong, D.-M. Tang, H. Li, T. Zhai, L. Li, Y. Bando and D. Golberg, *Adv. Funct. Mater.*, 2012, **22**, 2682–2690.

52 J. Y. Huang, L. Zhong, C. M. Wang, J. P. Sullivan, W. Xu, L. Q. Zhang, S. X. Mao, N. S. Hudak, X. H. Liu, A. Subramanian, H. Fan, L. Qi, A. Kushima and J. Li, *Science*, 2010, **330**, 1515–1520.

53 W. H. Shi, J. X. Zhu, D. H. Sim, Y. Y. Tay, Z. Y. Lu, X. J. Zhang, Y. Sharma, M. Srinivasan, H. Zhang, H. H. Hng and Q. Y. Yan, *J. Mater. Chem.*, 2011, **21**, 3422–3427.

54 Y. Ma, C. Zhang, G. Ji and J. Y. Lee, *J. Mater. Chem.*, 2012, **22**, 7845–7850.